

Elucidating the event-by-event flow fluctuations in heavy-ion collisions via the event shape selection technique

Peng Huo,¹ Jianguong Jia,^{1,2,*} and Soumya Mohapatra¹

¹*Department of Chemistry, Stony Brook University, Stony Brook, NY 11794, USA*

²*Physics Department, Brookhaven National Laboratory, Upton, NY 11796, USA*

The existence of higher-order flow and event-by-event flow fluctuations in heavy ion collisions at the RHIC and LHC offer a opportunity to study a broad class of flow observables. This paper explores two types of correlations involving harmonic flow coefficients v_n and their phases Φ_n : probability distributions $p(v_n, v_m)$ and $p(v_n, \Phi_m, \Phi_l, \dots)$, as well as the rapidity fluctuation of flow using the Pb+Pb events generated by the AMPT model with fixed impact parameter. The overall ellipticity or triangularity of events are varied by selecting on the eccentricities ϵ_n or the magnitudes of the flow vector q_n in a subevent for $n = 2$ and 3 , respectively. The responses of the v_m , the event plane correlation, and the rapidity fluctuations, to the change in ϵ_n and q_n are then systematized. Strong positive correlations are observed among all even harmonics v_2, v_4 , and v_6 (all increase with q_2), between v_2 and v_5 (both increase with q_2) and between v_3 and v_5 (both increase with q_3), consistent with the effects of non-linear hydrodynamic response. In contrast, an anti-correlation is observed between v_2 and v_3 similar to that seen between ϵ_2 and ϵ_3 . These correlation patterns are found to be independent of whether selecting on q_n or ϵ_n , validating the ability of q_n in selecting the initial geometry. A forward/backward asymmetry of $v_n(\eta)$ is observed for events selected on q_n but not on ϵ_n , reflecting dynamical fluctuation effects exposed by q_n selection. Many event plane correlators show good agreement between q_n and ϵ_n selections, suggesting that their variations with q_n reflect mainly the hydrodynamic response to the change of ϵ_n in the initial geometry. Hence these correlators may serve as promising observables for disentangling the fluctuations generated in various stages of the evolution of the matter created in heavy ion collisions.

PACS numbers: 25.75.Dw

I. INTRODUCTION

High energy heavy ion collisions at the RHIC and the LHC have created a new form of nuclear matter comprised of deconfined, yet strongly interacting quarks and gluons. This matter exhibits strong collective and anisotropic flow in the transverse plane, which is well described by relativistic hydrodynamics. The magnitude of the anisotropic flow has been found to be sensitive to the transport properties, as well as the space-momentum profile in the initial state. A central goal of current research is to understand the nature of various fluctuations in the initial state and how these fluctuations influence the hydrodynamic evolution of the matter in the final state.

In heavy ion collisions, the anisotropy of the particle distribution in azimuthal angle ϕ is customarily characterized by a Fourier series:

$$\frac{dN}{d\phi} \propto 1 + 2 \sum_{n=1}^{\infty} v_n \cos n(\phi - \Phi_n), \quad (1)$$

where v_n and Φ_n (event plane or EP) represent the magnitude and phase of the n^{th} -order harmonic flow. These flow harmonics have been associated to various shape components of the created matter. The magnitude and

direction of each shape component can be estimated via a simple Glauber model from the transverse positions (r, ϕ) of the participating nucleons [1, 2]:

$$\epsilon_n = \frac{\sqrt{\langle r^m \cos n\phi \rangle^2 + \langle r^m \sin n\phi \rangle^2}}{\langle r^m \rangle}, \quad (2)$$

$$\tan n\Phi_n^* = \frac{\langle r^m \sin n\phi \rangle}{\langle r^m \cos n\phi \rangle} + \frac{\pi}{n}, \quad (3)$$

$$m = 3 \text{ if } n = 1, m = n \text{ for } n > 1$$

with ϵ_n and Φ_n^* referred to as the eccentricity and participant plane (PP), respectively. Model calculations suggest that hydrodynamic response to the shape component is linear for the first few flow harmonics, i.e. $\Phi_n \approx \Phi_n^*$ and $v_n \propto \epsilon_n$ for $n = 1 - 3$. But these simple relations are violated for higher-order harmonics, due to strong non-linear mode-mixing effects intrinsic in the collective expansion [2-5].

The presence of large event-by-event (EbyE) fluctuations of the initial geometry suggests a general set of observables that involve correlations between v_n and Φ_n :

$$p(v_n, v_m, \dots, \Phi_n, \Phi_m, \dots) = \frac{1}{N_{\text{evts}}} \frac{dN_{\text{evts}}}{dv_n dv_m \dots d\Phi_n d\Phi_m \dots}, \quad (4)$$

with each variable being a function of p_T, η etc [6]. Among these, the joint probability distribution of the EP angles

$$\frac{dN_{\text{evts}}}{d\Phi_1 d\Phi_2 \dots d\Phi_l} \propto \sum_{c_n=-\infty}^{\infty} a_{c_1, c_2, \dots, c_l} \cos(c_1 \Phi_1 + c_2 \Phi_2 \dots + c_l \Phi_l),$$

$$a_{c_1, c_2, \dots, c_l} = \langle \cos(c_1 \Phi_1 + c_2 \Phi_2 + \dots + c_l \Phi_l) \rangle \quad (5)$$

*Correspond to jjia@bnl.gov

can be reduced to the following physical event plane correlators required by symmetry [7–9]:

$$\langle \cos(c_1\Phi_1 + 2c_2\Phi_2 \dots + l_l\Phi_l) \rangle, c_1 + 2c_2 \dots + l_l = 0. \quad (6)$$

These observables probe into the fluctuations in the initial density profile, as well as the linear and nonlinear hydrodynamics response to the profile [5].

Earlier flow measurements were aimed at studying the individual v_n coefficients for $n = 1-6$ averaged over many events [10–14]. Recently, the LHC experiments exploited the EbyE observables defined in Eq. 4 by performing the first measurement of $p(v_n)$ [15] for $n = 2-4$ and fourteen correlators involving two or three event planes [16, 17], in Pb+Pb collisions at $\sqrt{s_{NN}} = 2.76$ TeV. The measured event plane correlators are reproduced by EbyE hydrodynamics [18, 19] and AMPT transport model [20] calculations. The EP correlation measurement provide detailed insights on the non-linear hydrodynamic response, for example the correlators $\langle \cos 4(\Psi_2 - \Psi_4) \rangle$ and $\langle \cos 6(\Psi_3 - \Psi_6) \rangle$ mainly arise from the non-linear effects, which couple v_4 to $(v_2)^2$ and v_6 to $(v_3)^2$. Similarly, the correlator $\langle \cos(2\Psi_2 + 3\Psi_3 - 5\Psi_5) \rangle$ is driven by the non-linear coupling between v_5 and v_2v_3 [4, 5].

This paper focuses on two subsets of the observables defined by Eq. 4: $p(v_n, v_m)$ and $p(v_n, \Phi_m, \Phi_l, \dots)$, which can provide further insights on the linear and non-linear effects in the hydrodynamics response. The correlation $p(v_n, v_m)$ quantifies directly the coupling between v_m and v_n , while $p(v_n, \Phi_m, \Phi_l, \dots)$ allows us to study how the event plane correlations couples to a specific flow harmonics v_n . The probability distributions of these correlations are difficult to measure directly, instead we explore them systematically using the recently proposed event shape selection technique [21] (also investigated in Ref. [22, 23]): Events in a given centrality interval can be further classified according to the observed v_n signal in a subevent, and the $p(v_m)$ and $p(\Phi_m, \Phi_l, \dots)$ can then be measured precisely within each class. The event shape observables should be those that correlate well with the ϵ_n of the initial geometry, such as the observed v_1 (dipolar flow), v_2 and v_3 . The roles of these control observables are similar to the event centrality, except that they further divide events within the same centrality class.

The event shape selection technique also provides a unique opportunity to investigate the longitudinal dynamics of the collective flow. For example, events selected with large v_2 in one pseudorapidity window, in addition to bigger ϵ_2 , may also have stronger density fluctuations, larger initial flow or smaller viscous correction in this window [24]. Studying how the v_n values or EP correlations vary with the η separation from the selection window may provide better insights on the longitudinal dynamics in both the initial and the final states. Earlier efforts on this front can be found in Refs. [24–26].

In this paper, we apply the event shape selection technique to events generated by the AMPT model, to investigate the $p(v_n, v_m)$, $p(v_n, \Phi_m, \Phi_l, \dots)$, and the longitudinal flow fluctuations. These correlations are studied for

events binned according to the observed v_2/v_3 signal in the final state, which are then compared with results for events binned directly in ϵ_2/ϵ_3 . This comparison helps to elucidate whether the changes in the correlation are driven mostly by the selection of the initial geometry or whether there are additional dynamics in the final state exposed by the selection on v_2/v_3 . In addition to clarifying the connection between initial geometry and final state flow, the AMPT model also allow us to identify the most promising observables among the large set of EbyE observables for disentangling the fluctuations in various stages of the heavy ion collisions.

The structure of the paper is as follows: Section II introduces the observables and method of the event shape selection in the AMPT model. Section III studies how the correlations among the eccentricities and PP angles vary with event shape selection. Section IV presents a study of the rapidity fluctuations of flow. Section V studies how the correlations among the v_n and EP angles vary with event shape selection. Section VI gives a discussion and summary of the results.

II. THE METHOD

A Multi-Phase Transport model (AMPT) [27] has been used frequently to study the higher-order v_n associated with ϵ_n in the initial geometry [28–30]. It combines the initial fluctuating geometry based on Glauber model from HIJING and final state interaction via a parton and hadron transport model. The collective flow in this model is driven mainly by the parton transport. The AMPT simulations in this paper are performed with string-melting mode with a total partonic cross-section of 1.5 mb and strong coupling constant of $\alpha_s = 0.33$ [29], which has been shown to reproduce reasonably the experimental p_T spectra and v_n data at RHIC and LHC [29, 31]. The initial condition of the AMPT model with string melting has been shown to contain significant longitudinal fluctuations that can influence the collective dynamics [24, 32].

The AMPT sample used in this study is generated for $b = 8$ fm Pb+Pb collisions at LHC energy of $\sqrt{s_{NN}} = 2.76$ TeV, corresponding to $\sim 30\%$ centrality. The particles in each event are divided into various subevents along η , one example division scheme is shown in Figure 1. Four subevents labelled as S,A,B,C, with at least 1 unit η -gap between any pair except between S and A, are used in the analysis. Note that particles in $-6 < \eta < -2$ are divided randomly into two equal halves, labelled as S and A, respectively. The particles in subevent S are used only for the event shape selection purpose, and they are excluded explicitly for v_n and event plane correlation analysis. This choice of subevents and analysis scheme ensure that the event shape selection on subevent S do not introduce non-physical correlations between subevents A,B and C.

The flow vector in each subevent is calculated as:

$$\vec{q}_n = (q_{x,n}, q_{y,n}) = \frac{1}{\Sigma w} (\Sigma(w \cos n\phi), \Sigma(w \sin n\phi)) ,$$

$$\tan n\Psi_n = \frac{q_{y,n}}{q_{x,n}} , \quad (7)$$

where the weight w is chosen as the p_T of each particle and Ψ_n is the measured event plane. Due to finite number effects, Ψ_n smears around the true event plane angle Φ_n . In the limit of infinite particle multiplicity, the magnitude of the flow vector defined this way is equal to the weighted average of v_n : $(v_n)_w = \Sigma w v_n / \Sigma w$. In this study, each subevent in Figure 1 has 1400-3000 particles, so q_n is expected to follow closely the $(v_n)_w$.

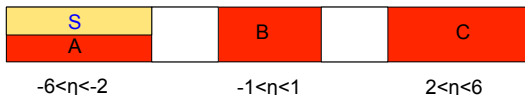


FIG. 1: (Color online) The η converges of the subevent for the event shape selection (S) and the other three subevents for correlation analysis (A,B and C). Note that the particles in $-6 < \eta < -2$ are divided randomly and equally into subevent A and S.

For each generated event, the following quantities are calculated for $n = 1 - 6$: (ϵ_n, Φ_n^*) from initial state, (q_n^A, Ψ_n^A) for subevent A, (q_n^B, Ψ_n^B) for subevent B, (q_n^C, Ψ_n^C) for subevent C, and (q_n^S, Ψ_n^S) for subevent S, a total of 64 quantities. The event shape selections are performed by dividing the generated events into 10 bins in q_2^S or q_3^S with equal statistics. Similar event shape selection are also performed by slicing the values of ϵ_2 or ϵ_3 directly, with the aim of studying how well the physics for events selected at final state correlates with those selected purely on the initial geometry.

Figure 2 shows the performance of the event shape selection on q_2^S and q_3^S . Strong positive correlations between ϵ_n and q_n^S seen in the top panels reflect the fact that hydrodynamic response is linear for $n = 2$ and 3 [18]. The bottom panels suggests events selected by the top 10% of the q_2^S has a $\langle \epsilon_2 \rangle$ value that is nearly 3 times that for events with the lower 10% of q_2^S . For $n = 3$ the difference in ϵ_3 in the two event classes is about a factor of 2. These results suggest that the ellipticity and triangularity of the initial geometry can be selected rather precisely by slicing the flow vector in the final state. Note that the distributions of q_n^S in the middle row of Figure 2 are dominated by real flow fluctuations in $(v_n)_w$, which is much larger than the statistical smearing associated with the finite number of particles in subevent A (about 1400).

In the event shape selection technique, $p(v_m, v_n)$ is not directly calculated. Instead, the calculated correlation is:

$$p(q_m^S, v_n^{\text{obs}}) = p(q_m^S) \times p(v_n^{\text{obs}})_{q_m^S}, \quad m = 2, 3 \quad (8)$$

where conditional probability $p(v_n^{\text{obs}})_{q_m^S}$ represents the distribution of v_n^{obs} for events selected with given q_m^S values. To minimize non-flow effects, the v_n^{obs} is calculated

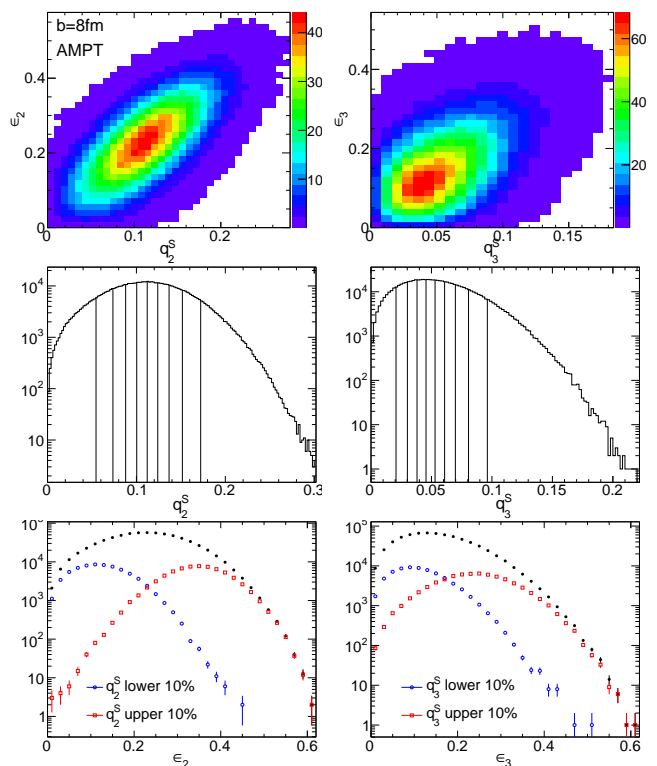


FIG. 2: (Color online) The correlation between ϵ_n and magnitude of flow vector q_n^S calculated using half of the particles in $-6 < \eta < -2$ (Top panels), the 10 bins in q_n^S with equal statistics (middle panels) and the corresponding distribution of ϵ_n for events in the top 10%, bottom 10% and total of q_n^S (bottom panels). The results are calculated for $b = 8$ fm for $n = 2$ and $n = 3$, and are shown in the left and right column, respectively.

for particles separated in η from the subevent that provides the event plane. To minimize non-flow effects, a η -gap from the corresponding event plane in each case is required. The probability $p(v_n)_{q_m^S}$ can be obtained from $p(v_n^{\text{obs}})_{q_m^S}$ via the unfolding technique [15, 33], or if one is interested in the event averaged v_n values, the standard method [34] can be applied for each q_m^S bin:

$$v_n(p_T, \eta)_{q_m^S} = \left[\frac{v_n^{\text{obs}}(p_T, \eta)}{\text{Res}\{n\Psi_n\}} \right]_{q_m^S}, \quad (9)$$

where the event plane resolution factor $\text{Res}\{n\Psi_n\}$ is calculated separately for A,B, and C via the three-subevent method, providing three independent v_n estimates [34]. Since the value of q_m^S are not correlated with event plane angle Ψ_n^S , the event shape selection is not expected to introduce non-physical biases to the resolution correction. One special case of Eq. 9 is $n = m$, which probes into the rapidity fluctuation of the v_n itself (see Section IV).

To calculate the event plane correlation for each q_m^S bin, the standard method introduced by the ATLAS collaboration based on event plane correlation [9, 16], and the method based on scalar products in Refs. [20, 35] are

used:

$$\langle \cos(\Sigma\Phi) \rangle = \frac{\langle \cos(\Sigma\Psi) \rangle}{\text{Res}\{c_1\Psi_1\}\text{Res}\{c_2\Psi_2\}\dots\text{Res}\{c_l\Psi_l\}} \quad (10)$$

$$\langle \cos(\Sigma\Phi) \rangle_w = \frac{\langle q_1^{c_1} q_2^{c_2} \dots q_l^{c_l} \cos(\Sigma\Psi) \rangle}{\text{Res}\{c_1\Psi_1\}_w \text{Res}\{c_2\Psi_2\}_w \dots \text{Res}\{c_l\Psi_l\}_w} \quad (11)$$

where shorthand notions $\Sigma\Phi = c_1\Phi_1 + 2c_2\Phi_2 + \dots + lc_l\Phi_l$ and $\Sigma\Psi = c_1\Psi_1 + 2c_2\Psi_2 + \dots + lc_l\Psi_l$ are used. They are referred to as the EP method (Eq. 10) and the SP method (Eq. 11) for the rest of this paper. The resolution factors $\text{Res}\{c_n n\Psi_n\}$ and $\text{Res}\{c_n n\Psi_n\}_w$ are calculated via three-subevent method involving subevents A, B and C:

$$\text{Res}\{jn\Psi_n^A\} = \sqrt{\frac{\langle \cos \Delta\Psi_n^{AB} \rangle \langle \cos \Delta\Psi_n^{AC} \rangle}{\langle \cos \Delta\Psi_n^{BC} \rangle}}. \quad (12)$$

$$\text{Res}\{jn\Psi_n^A\}_w = \sqrt{\frac{\langle (q_n^A q_n^B)^j \cos \Delta\Psi_n^{AB} \rangle \langle (q_n^A q_n^C)^j \cos \Delta\Psi_n^{AC} \rangle}{\langle (q_n^B q_n^C)^j \cos \Delta\Psi_n^{BC} \rangle}}. \quad (13)$$

where $\Delta\Psi_n^{AB} = jn(\Psi_n^A - \Psi_n^B)$ etc. Each Ψ_n angle in Eq. 11 is calculated in a separate subevent to avoid auto-correlations. The two subevents involved in two-plane correlation are chosen as A and C in Figure 1, while three subevents in three-plane correlation are chosen as A,B,and C in Figure 1. Note that the selection on q_n^S explicitly breaks the symmetry between subevents A and C even though they still have symmetric η acceptance. Thus their resolution factors are different and need to be calculated separately.

III. CORRELATIONS IN THE INITIAL STATE

Before discussing correlations in the final state, it is instructive to look first at how the initial geometry variables ϵ_n, Φ_n^* and their correlations vary with the event shape selection. Figure 3 shows the correlations between pairs of ϵ_n for $n \leq 4$ for the generated AMPT events. Significant correlations are observed between ϵ_2 and ϵ_3 [23], ϵ_1 and ϵ_3 . The correlations between ϵ_1 and ϵ_2 are weak for this impact parameter but become more significant for $b = 10$ fm (see Appendix A). Since the hydrodynamic response is nearly linear for $n = 1 - 3$ [3], these correlations are expected to survive into correlations between v_n of respective order. The ϵ_2 and ϵ_4 correlation is also significant, especially for large ϵ_2 values, this correlation may survive to the final state but it will compete with non-linear effects expected for v_4 [4].

Figure 4 shows selected correlations between Φ_n^* of different order for events binned in ϵ_2 (boxes) or q_2^S (circles) [9, 36]. It is clear that the correlation signal varies dramatically with ϵ_2 , implying that the relative angles between Φ_n^* can vary a lot for events with the same impact parameter. Figure 4 also shows that events with

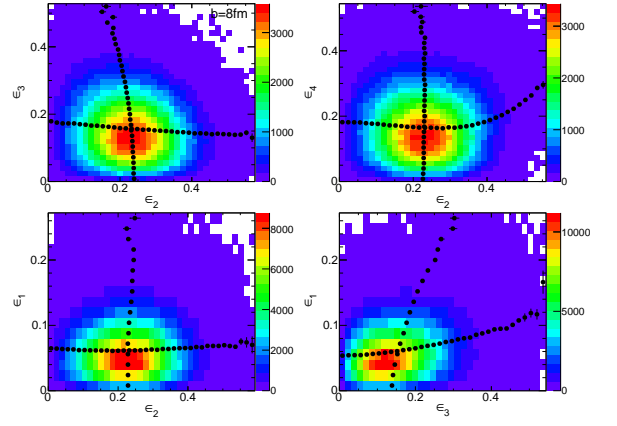


FIG. 3: (Color online) Selected correlations between ϵ_n of different order for Pb+Pb events generated at $b = 8$ fm. More correlation examples are given in Appendix A. The x - and y -profiles of the 2D correlations are represented by the solid symbols.

different correlations in the initial geometry can be selected with nearly the same precision between using q_2^S and using ϵ_2 .

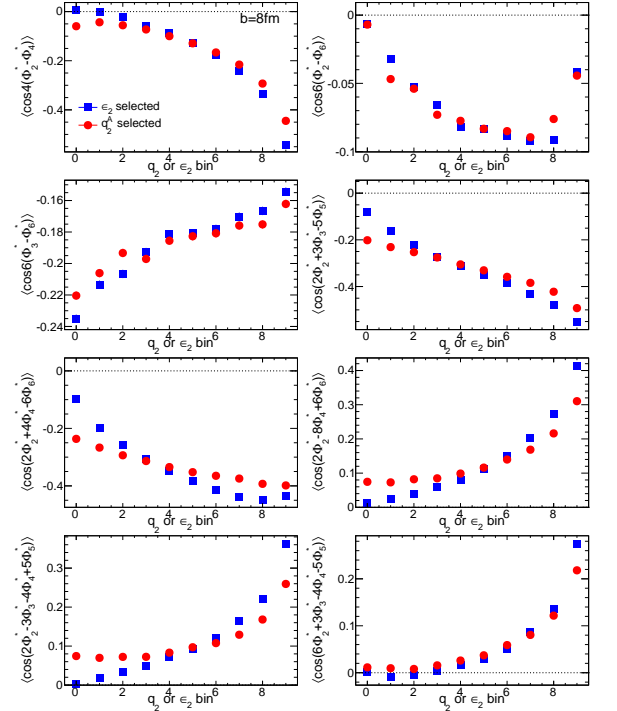


FIG. 4: (Color online) Dependence of the participant plane angle correlations on the ϵ_2 (boxes) or q_2^S (circles), calculated for Pb+Pb events generated at $b = 8$ fm. Results for three two-plane, three three-plane and two four-plane correlators proposed in Refs. [9, 36] are shown.

IV. THE CORRELATION BETWEEN v_n AND v_m AND LONGITUDINAL FLUCTUATIONS

Figure 5 shows the $v_2(\eta)$ values for events selected for lower 10% (top panels) and upper 10% (bottom panels) of the values of either q_2^S (left panels) or ϵ_2 (right panels). They are calculated via Eqs. 9 and 12 using all final state particles with $0.1 < p_T < 5$ GeV, excluding those particles used in the event shape selection (i.e. subevent S). The event plane angles are calculated separately for the three subevents A, B, and C, and a minimum 1-2 unit of η gap is required between $v_n(\eta)$ and the subevent used to calculate the event plane. Specifically, the v_2 values in $-6 < \eta < 0$ are obtained using the EP angle in subevent C covering $2 < \eta < 6$ (open boxes), the v_2 values in $0 < \eta < 6$ are obtained using the EP angle in subevent A covering $-6 < \eta < -2$ (open circles), and the v_2 values in $|\eta| > 2$ are also obtained using the EP angle in subevent B covering $|\eta| < 1$ (solid circles).

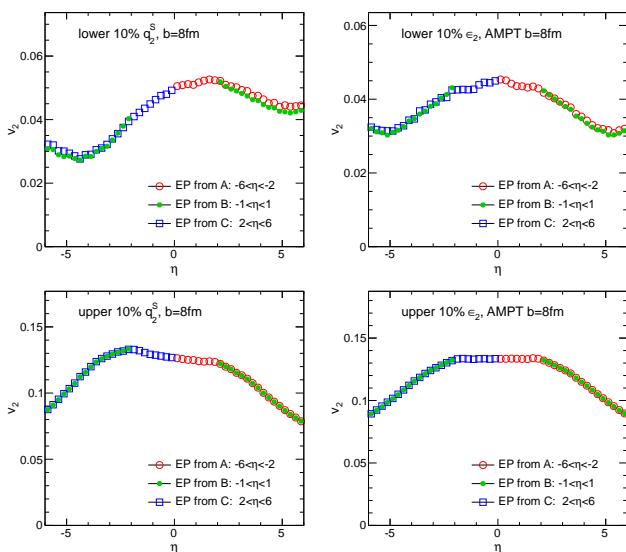


FIG. 5: (Color online) The η dependence of the v_2 for events selected with lower 10% (top panels) and upper 10% (bottom panels) of the values of either q_2^S (left panels) or ϵ_2 (right panels) for AMPT Pb+Pb events with $b = 8$ fm. In each case, the integral v_2 calculated for particles in $0.1 < p_T < 5$ GeV relative to the event plane of subevent A, B and C (Their η coverages are indicated in the legend) with a minimum η -gap of 1 unit are shown.

There are several interesting features in the observed η dependence of v_2 . The $v_2(\eta)$ values for events selected with lower 10% values of q_2^S or ϵ_2 is significantly lower (by a factor of 3) than that selected with upper 10%, indicating that the v_2 signal correlates well with both the q_2^S and ϵ_2 . Furthermore, a significant forward/backward asymmetry of $v_2(\eta)$ is observed for events selected on q_2^S but not ϵ_2 . This asymmetry is already observed outside the η range covered by subevent S, but is bigger towards larger $|\eta|$. This asymmetry may reflect the dynamical

fluctuations of flow in the final state exposed by the q_2^S selection. Additional cross-checks performed by choosing subevent S in a more restricted η range also show this asymmetry (see Figure 16 in the Appendix).

Based on the good agreement between the three v_2 estimations in Figure 5, they are combined into a single $v_2(\eta)$ result. Good agreement is also observed for higher harmonics, hence they are combined in the same way. The resulting $v_2(\eta) - v_6(\eta)$ are shown in Figure 6 for events with lower 10% and upper 10% of the values of q_2^S . The asymmetry of v_n in η is much weaker for the higher-order harmonics. The values of $v_n(\eta)$ for $n > 3$ are also seen to be positively correlated with v_2 , i.e. events with large q_2^S also have bigger $v_n(\eta)$. On the other hand, v_3 values are observed to decrease with increasing q_2^S . This decrease may just reflect the anti-correlation between ϵ_2 and ϵ_3 in Figure 3. Figure 7 quantifies the forward/backward asymmetry of $v_2 - v_6$ in two η ranges: $-5 < \eta < -4$ and $4 < \eta < 5$. Clear asymmetry can be seen for v_2 , v_4 and v_5 , but not for v_3 . This behavior re-enforces our earlier conclusion that the correlation between v_2 and v_3 in the AMPT model is mostly geometrical, i.e. reflecting correlation between ϵ_2 and ϵ_3 .

An identical analysis is also performed for events selected on the q_3^S or ϵ_3 . The $v_n(\eta)$ for events with the upper 10% and lower 10% values of q_3^S or ϵ_3 are shown in Figure 8. A strong η asymmetry is observed as a result of q_3^S selection, but not for ϵ_3 selection. Nevertheless, the overall magnitudes of the v_3 are similar between the two selections. In the $-6 < \eta < -2$ range where q_3^S is calculated, $v_3(\eta)$ values for events with the lower 10% of q_3^S drop to below zero. This implies that the Φ_3 angle for large negative η region become totally out of phase with the Φ_3 angle in the large positive range. This Φ_3 angle decorrelation is also observed for events selected with lower 10% of ϵ_3 values as shown in the top right panel of Figure 8: v_3 values at large $|\eta|$ are close to zero or negative and differ significantly between different estimates. This behavior suggests that in the AMPT model, rapidity decorrelation of v_3 is stronger for events with small ϵ_3 and grows towards large $|\eta|$ (negative v_3 implies its phase is totally opposite to that in the η region used to obtain the event plane). An earlier study [26] has shown evidences of η decorrelation of v_3 in the AMPT; our studies here suggest such decorrelation effects are better exposed and hence are easier to study for events selected with small q_3^S or ϵ_3 .

Figure 9 quantifies the rapidity asymmetry of v_n between $-5 < \eta < -4$ and $4 < \eta < 5$ as a function of q_3^S and ϵ_3 . The even harmonics v_2 and v_4 show little asymmetry and are nearly independent of q_3^S . In contrast, the v_5 values show a strong η -asymmetry that is totally correlated with the asymmetry of v_3 . The correlation between v_3 and v_5 is stronger than that between v_2 and v_5 seen in Figure 7, suggesting that the hydrodynamic non-linear coupling between v_5 and v_3 is stronger (this is further supported by the behavior of $\langle \cos(2\Psi_2 + 3\Psi_3 - 5\Psi_5) \rangle$ between Figure 14 and Figure 15).

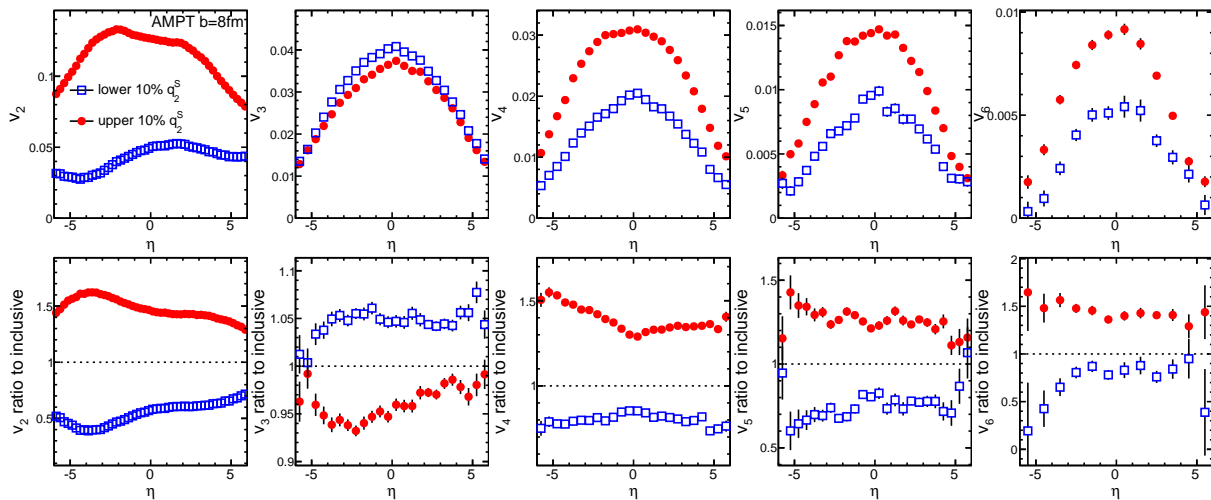


FIG. 6: (Color online) $v_n(\eta)$ for events selected with lower 10% (open symbols) and upper 10% (solid symbols) of the values of q_2^S for AMPT Pb+Pb events with $b = 8$ fm. Results are shown for $v_2(\eta)$, $v_3(\eta)$... $v_6(\eta)$ from left panel to the right panel. The ratios of $v_n(\eta)$ between events with q_2^S selection to the inclusive events are shown in the bottom panels.

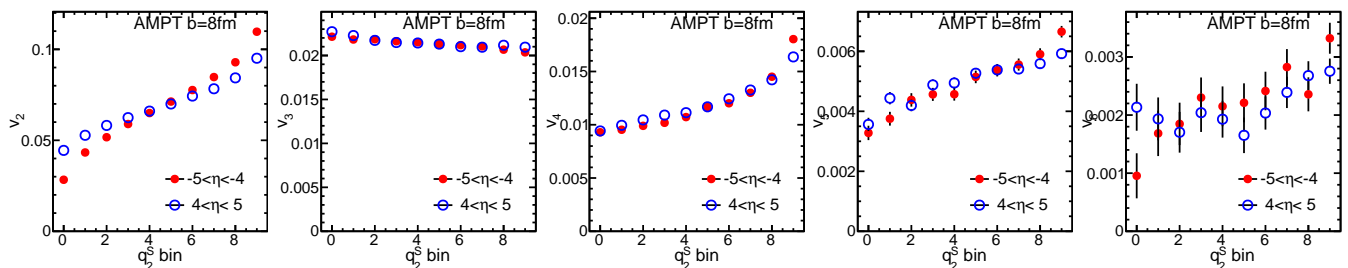


FIG. 7: (Color online) Dependence of the v_n on q_2^S in a forward ($-5 < \eta < -4$) and a backward ($4 < \eta < 5$) pseudorapidity ranges.

Figure 10 shows the particle multiplicity distributions $dN/d\eta$ for events selected on q_2^S (left) or q_3^S (right). The distributions remain largely symmetric in η and the overall magnitude is nearly independent of the event selection. We also verified explicitly the number of participating nucleons N_{part} for the projectile and target are nearly equal for all q_2^S or q_3^S bins. This suggests the mechanism responsible for the rapidity fluctuation of flow observed in the AMPT model is not due to the mechanism proposed by Bzdak and Teaney [37].

V. EVENT PLANE CORRELATIONS

The AMPT model have been shown to reproduce [20] the centrality dependence of various two-plane and three-plane correlations measured by the ATLAS Collaboration [16]. Here we use AMPT model to study how these correlators change with q_n^S or ϵ_n for events with fixed impact parameter. In this analysis, the two-plane correlators $\langle \cos k(\Phi_n - \Phi_m) \rangle$ are calculated by correlating the EP angles from subevent A and subevent C. Each subevent provides its own estimation of the EPs: Ψ_n^A

and Ψ_m^A from subevent A and Ψ_n^C and Ψ_m^C from subevent C. This leads to two statistically independent estimates of the correlator: Type1 $\langle \cos k(\Phi_n^A - \Phi_m^C) \rangle$ and Type2 $\langle \cos k(\Phi_n^C - \Phi_m^A) \rangle$. The two estimates are identical for events selected on ϵ_2 , and hence they are averaged to obtain the final result. But for events selected based on q_2^S , the two estimates can differ quite significantly.

Figure 11 shows the values of four two-plane correlators in bins of q_2^S or ϵ_2 . The values of the correlators are observed to increase strongly with increasing q_2^S or ϵ_2 . The two estimates based on q_2^S selection differ significantly, reflecting the influence of longitudinal flow fluctuations exposed by the q_2^S selection. Interestingly, the correlators whose Φ_2 angle is calculated in subevent C agrees very well with those based on ϵ_2 event shape selection, such as $\langle \cos 4(\Phi_2^C - \Phi_4^A) \rangle$. This is because Φ_2^C , Φ_4^A and Φ_4^C are expected to be less dependent on the q_2^S selection than Φ_2^A (see the response of v_4 to q_2^S shown in Figure 7). These observations suggest that the dependence of $\langle \cos 4(\Phi_2^C - \Phi_4^A) \rangle$ and $\langle \cos 6(\Phi_2^C - \Phi_6^A) \rangle$ on q_2^S reflects mainly the change in the initial geometry and the ensuing non-linear effects in the final state. Note that the last bin in each panel represents the value obtained

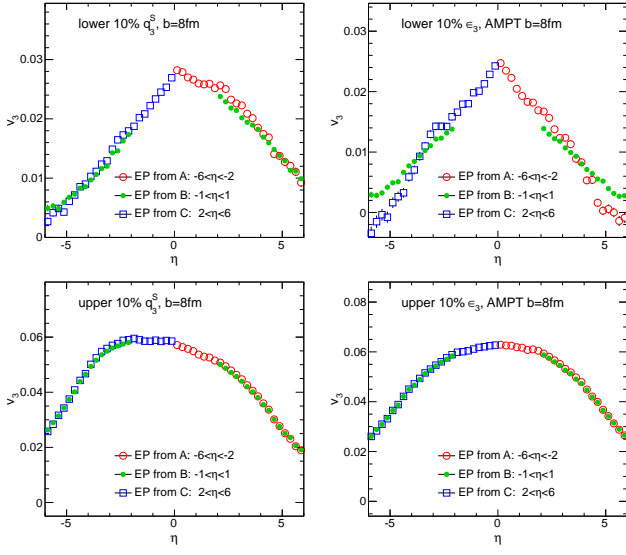


FIG. 8: (Color online) The η dependence of the v_3 for events selected for lower 10% (top panels) and upper 10% (bottom panels) of the values of either q_3^S (left panels) or ϵ_3 (right panels) for AMPT Pb+Pb events with $b = 8$ fm. In each case, the integral v_3 calculated for particles in $0.1 < p_T < 5$ GeV relative to the event plane of subevent A, B and C (Their η coverages are indicated in the legend) with a minimum η -gap of 1 unit are shown.

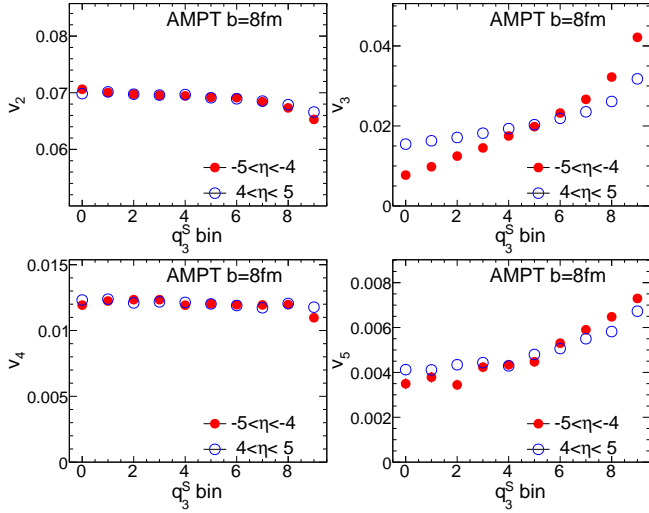


FIG. 9: (Color online) Dependence of the v_n on q_3^S in a forward ($-5 < \eta < -4$) and a backward ($4 < \eta < 5$) pseudorapidity ranges.

without event shape selection, which agrees between the three calculations by construction.

Figure 12 compares various two-plane correlators calculated via the EP method and the SP method given by Eqs. 10-13. The SP method is observed to give systematically higher values for Type1 correlators where the first angle is measured by subevent A, while it gives consist-

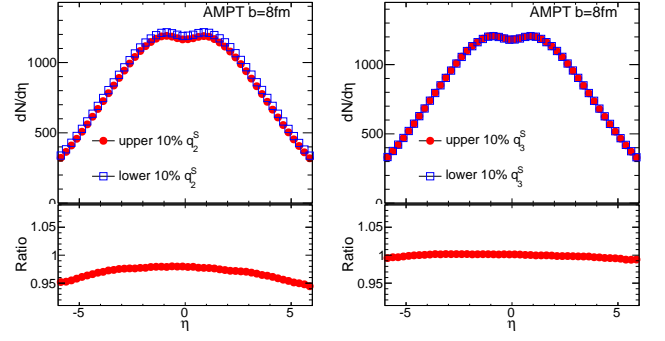


FIG. 10: (Color online) The $dN/d\eta$ distributions of all particles for events selected on q_2^S (left) and q_3^S (right).

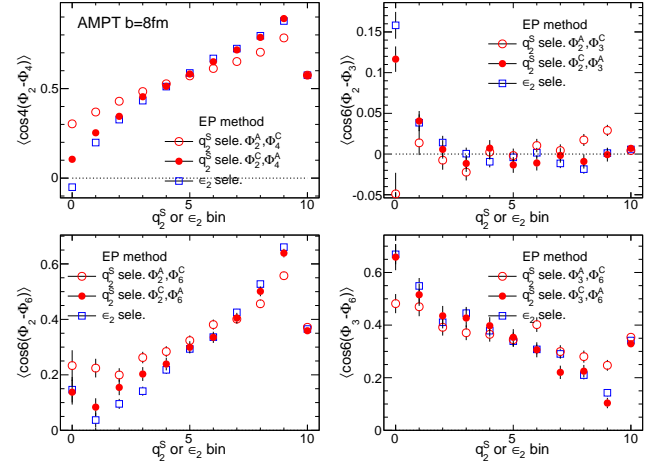


FIG. 11: (Color online) The four two-plane correlations as a function of bins of q_2^S or ϵ_2 for AMPT Pb+Pb events with $b = 8$ fm. The two event planes Φ_n and Φ_m are measured by subevent A and subevent C. The q_2^S -binned results are presented separately for the two combinations: $\langle \cos k(\Phi_n^A - \Phi_m^C) \rangle$ (open circles) and $\langle \cos k(\Phi_n^C - \Phi_m^A) \rangle$ (solid circles).

tent or slightly lower values for Type2 correlators. The last bin in each panel shows the result obtained without event shape selection, where the SP method is observed to always give higher values as expected [20].

Figure 13 shows $\langle \cos 6(\Phi_2 - \Phi_3) \rangle$ and $\langle \cos 6(\Phi_3 - \Phi_6) \rangle$ in bins of q_3^S or ϵ_3 . The first correlator shows little dependence on q_3^S or ϵ_3 , while the second correlator does. This is in sharp contrast to the results seen in Figure 11, where both correlators show strong but opposite dependence on q_2^S or ϵ_2 . This behavior is consistent with a strong non-linear coupling between v_6 and v_2 , v_6 and v_3 , but weak coupling between v_2 and v_3 .

To calculate three-plane correlations, subevents A, B and C are used. Each subevent provides its own estimation of the three EP angles, and hence there are $3! = 6$ independent ways of estimating the same three-plane correlator. For $c_n n \Phi_n + c_m m \Phi_m + c_l l \Phi_l$ with $n < m < l$, these six estimates are labelled as the following:

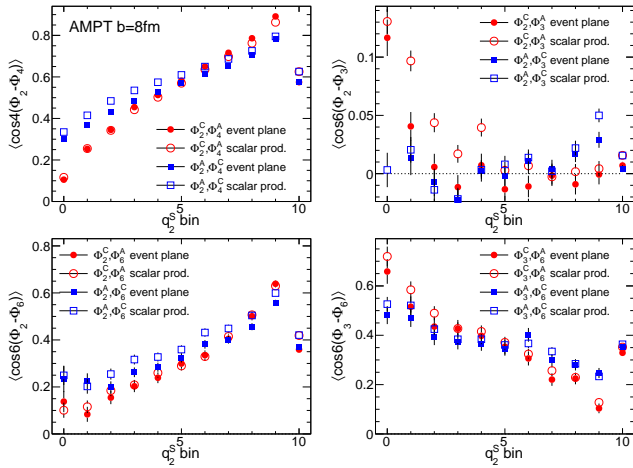


FIG. 12: (Color online) The four two-plane correlators in bins of q_2^S for AMPT Pb+Pb events with $b = 8$ fm, shown for two different combinations of the event plane angles (solid symbols), and compared with the correlation calculated via the scalar product method (open symbols).

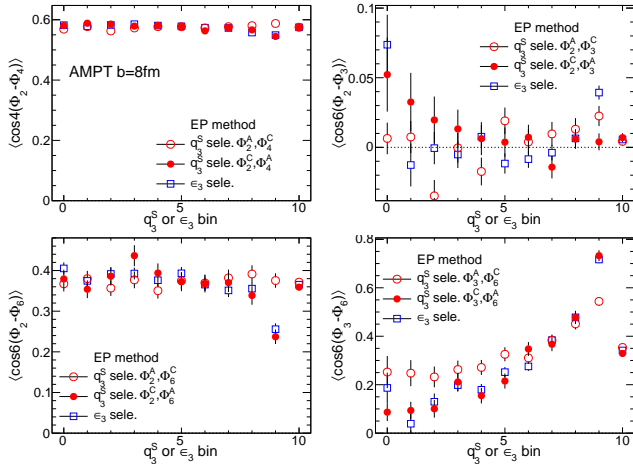


FIG. 13: (Color online) Two two-plane correlators as a function of either q_3^S or ϵ_3 for AMPT Pb+Pb events with $b = 8$ fm. The event planes Φ_n and Φ_m are measured by subevent A and subevent C. The q_3^S -binned results are presented separately for the two estimates: $\langle \cos k(\Phi_n^A - \Phi_m^C) \rangle$ (open circles) and $\langle \cos k(\Phi_n^C - \Phi_m^A) \rangle$ (solid circles).

- Type 1a: $c_n n \Phi_n^B + c_m m \Phi_m^A + c_l l \Phi_l^C$
- Type 1b: $c_n n \Phi_n^B + c_m m \Phi_m^C + c_l l \Phi_l^A$
- Type 2a: $c_n n \Phi_n^A + c_m m \Phi_m^B + c_l l \Phi_l^C$
- Type 2b: $c_n n \Phi_n^C + c_m m \Phi_m^B + c_l l \Phi_l^A$
- Type 3a: $c_n n \Phi_n^A + c_m m \Phi_m^C + c_l l \Phi_l^B$
- Type 3b: $c_n n \Phi_n^C + c_m m \Phi_m^A + c_l l \Phi_l^B$

For events selected on ϵ_n , the symmetry of the η -coverage between A and C reduces them into three equivalent pairs

of estimates. However for events selected on q_n^S , all six estimates can be different.

Figure 14 summarizes the results for five three-plane correlators, one for each column, calculated for events classified by q_2^S or ϵ_2 ¹, including a previously unnoticed strong correlator $\langle \cos(2\Phi_2 - 8\Phi_4 + 6\Phi_6) \rangle$. The six estimates of each correlator are grouped into three pairs and are shown in the three rows. Many of these correlators exhibit a breaking of the symmetry between subevent A and C, see for example the Type1 and Type2 for the first two correlators, as well as the Type1 and Type3 for the third and fourth correlators. Some correlators even show opposite dependence on q_2^S , such as the Type1 and Type3 for the fourth correlator ($\langle \cos(2\Phi_2 - 6\Phi_3 + 4\Phi_4) \rangle$). In most cases, however, the overall dependences on ϵ_2 bin (open circles) are reasonably captured by the dependence on q_2^S (open boxes), implying that these correlations reflect mainly the intrinsic hydrodynamic response to the change in the selected initial geometry.

Figure 15 summarizes the results for the same five three-plane correlators, but calculated for events classified by q_3^S or ϵ_3 . Comparing with Figure 14, we find that the values of $\langle \cos(2\Phi_2 - 3\Phi_3 + 5\Phi_5) \rangle$ are more sensitive to q_3^S or ϵ_3 than to q_2^S or ϵ_2 for small bin numbers, possibly reflecting stronger rapidity decorrelation effects associated with Φ_3 seen for small q_3^S or ϵ_3 in Figure 8. The correlators $\langle \cos(2\Phi_2 - 6\Phi_3 + 4\Phi_4) \rangle$ and $\langle \cos(2\Phi_2 + 6\Phi_3 - 8\Phi_4) \rangle$ show better agreement between the six types than when they are selected by q_2^S or ϵ_2 as shown in Figure 14, again reflecting the weak correlation between v_3 and v_2 , and between v_3 and v_4 .

VI. DISCUSSION AND SUMMARY

This paper studies two sets of flow observables involving the correlation between harmonic flow coefficients v_n and their phases Φ_n : $p(v_n, v_m)$ and $p(v_n, \Phi_m, \Phi_l, \dots)$, utilizing the recently proposed event shape selection technique [21]. The shape of the collision geometry is selected by cutting on q_n (the magnitude of the flow vector in a subevent) and eccentricity ϵ_n . The $p(v_m)$ or the differential distribution of event-averaged v_m , and the event plane correlations $p(\Phi_m, \Phi_l, \dots)$ can then be studied in each q_n or ϵ_n bin. A special case of interest is to measure the $v_n(\eta)$ for events selected on q_n , which could be sensitive to rapidity fluctuations of collective flow. The feasibility of measuring these new observables is investigated using the AMPT model. This model combines the Glauber initial fluctuating geometry with collective flow generated by partonic transport, and hence allows

¹ We also calculate these correlators using the SP method (a.l.a. q_n -weights), the dependences on q_2^S are found to be qualitatively the same, though the overall magnitudes may differ (see Figure 20).

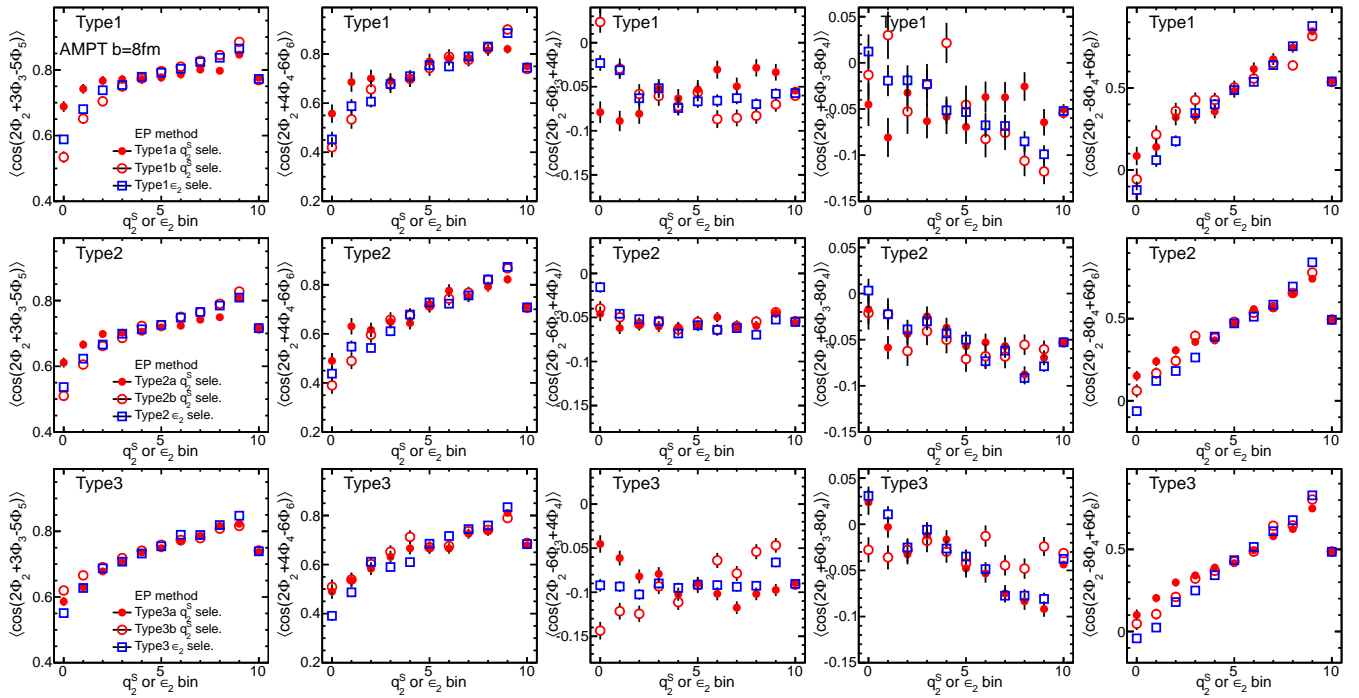


FIG. 14: (Color online) The five three-plane correlators (from left to right) as a function of either q_2^S (solid symbols) or ϵ_2 (open symbols) for AMPT Pb+Pb events with $b = 8$ fm. The results for the three type groups are shown in different row: Type1a and Type1b (top row), Type2a and Type2b (middle row), Type2a and Type2b (bottom row). The last bin in each panel shows the inclusive result.

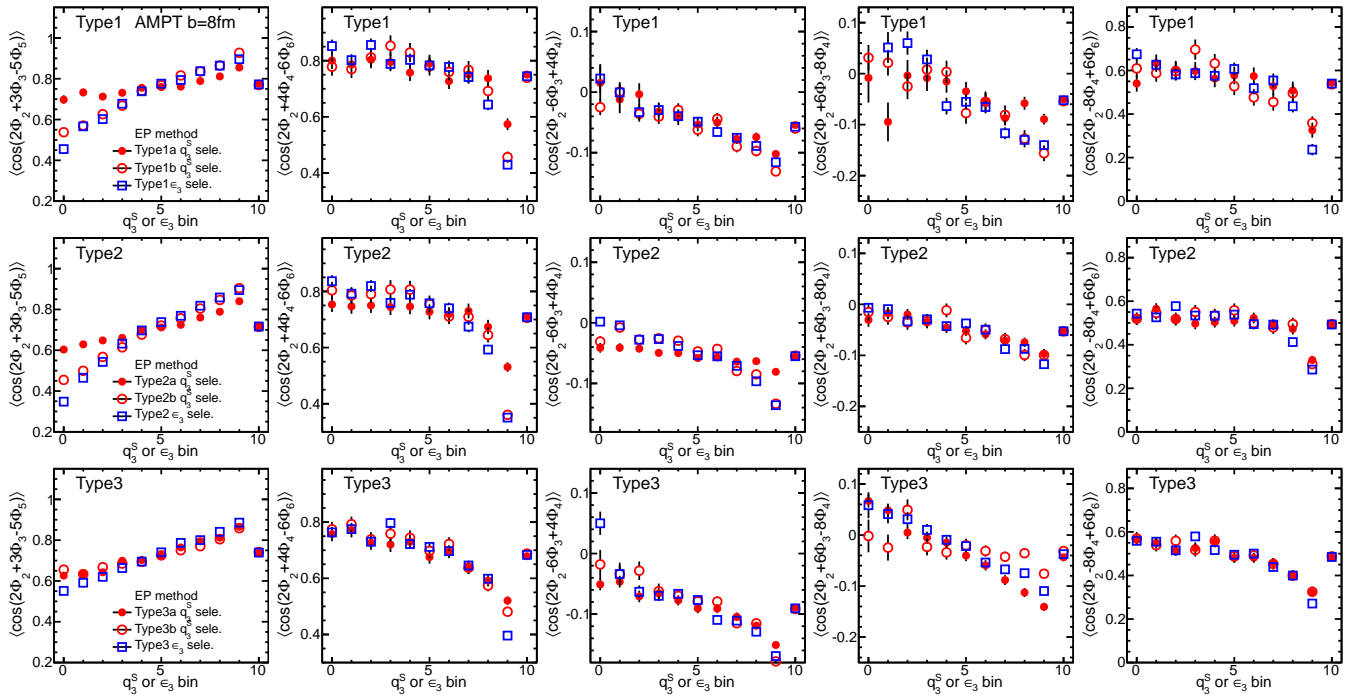


FIG. 15: (Color online) The five three-plane correlators (from left to right) as a function of either q_3^S (solid symbols) or ϵ_3 (open symbols) for AMPT Pb+Pb events with $b = 8$ fm. The results for the three type groups are shown in different row: Type1a and Type1b (top row), Type2a and Type2b (middle row), Type2a and Type2b (bottom row). The last bin in each panel shows the inclusive result.

one to correlate the initial geometry information, *e.g.* (ϵ_n, Φ_n^*) , with the (v_n, Φ_n) on a EbyE basis. Since the AMPT

model describes reasonably the experimentally measured p_T spectra, v_n [29, 31], and event plane correlations [20], it should provide a good benchmark for the performance of event shape selection, as well as provide qualitative and quantitative understanding of the physics behind these new observables.

To summarize, this study has been performed for Pb+Pb collisions at $\sqrt{s_{NN}} = 2.76$ TeV with fixed impact parameter $b = 8$ fm, which corresponds to $\sim 30\%$ centrality. The event shape selection is performed on the q_2^S and q_3^S calculated using half of the particles in $-6 < \eta < -2$, as well as on ϵ_2 and ϵ_3 to benchmark the performance of event shape selection. The EP angles used to calculate the EP correlators are calculated in subevent A (the other half particles in $-6 < \eta < -2$), subevent B covering $-1 < \eta < 1$ and subevent C covering $2 < \eta < 6$. Our main findings can be summarized below:

- The eccentricity ϵ_n distribution is very broad for events with fixed impact parameter and correlates well with q_n for $n = 2$ and 3, hence the events with different ellipticity or triangularity can be selected precisely using the q_2 and q_3 respectively.
- The participant plane correlations, such as $\langle \cos 4(\Phi_2^* - \Phi_4^*) \rangle$, $\langle \cos 6(\Phi_2^* - \Phi_6^*) \rangle$ and $\langle \cos 6(\Phi_3^* - \Phi_6^*) \rangle$, are observed to vary strongly with ϵ_2 or ϵ_3 , and much of these dependences are preserved when selecting on q_2 or q_3 .
- Significant correlations or anti-correlations are observed among the ϵ_n , such as $p(\epsilon_2, \epsilon_3)$, $p(\epsilon_1, \epsilon_3)$ and $p(\epsilon_2, \epsilon_4)$. These correlations can be easily probed by the event shape selection technique, some of these correlations, *e.g.* $p(\epsilon_1, \epsilon_3)$ and $p(\epsilon_2, \epsilon_3)$, are expected to survive to the final state. Indeed, the correlation between ϵ_2 and ϵ_3 seems to be reflected by the observed correlation between v_2 and v_3 in the AMPT model.
- The overall v_n values in each q_n^S bin are similar to that in the corresponding ϵ_n bin ($n = 2$ and 3). However a strong forward/backward asymmetry of $v_n(\eta)$ is observed in q_n^S selected events (also v_4, v_5 for q_2^S and v_5 for q_3^S), reflecting the dynamical fluctuations either in the initial state (initial flow [24, 38]) or during the collective expansion present in the AMPT model. These dynamical fluctuations are exposed by the q_n^S selection, probably because they are either short range in η or have strong η dependence. These dynamical effects also contribute strongly to event plane decorrelations. We also observe that the shape and values of $dN/d\eta$ are not affected much by the event shape selection.
- The v_n are always positively correlated with q_n^S , however other harmonics v_m , $m \neq n$ show non-trivial dependence on q_n^S . For q_2^S selection, v_4, v_5 and v_6 show positive correlation, while v_3 shows

negative correlation consistent with the behavior of $p(\epsilon_2, \epsilon_3)$. For q_3^S selection, v_5 shows positive correlation, while the v_2 and v_4 show slight negative correlation. These correlations are qualitatively consistent with non-linear couplings between different harmonics expected for collective flow [5].

- The strengths of several event plane correlators vary strongly with q_n^S and ϵ_n . These variations are observed to be similar between the EP method and the SP method. In many cases, they are also found to be similar between q_n^S selection and ϵ_n selection, namely the $\langle \cos 4(\Phi_2^C - \Phi_4^A) \rangle$, $\langle \cos 6(\Phi_2^C - \Phi_6^A) \rangle$, and many of $\langle \cos(2\Phi_2 + 3\Phi_3 - 5\Phi_5) \rangle$, $\langle \cos(2\Phi_2 + 4\Phi_4 - 6\Phi_6) \rangle$ and $\langle \cos(2\Phi_2 - 8\Phi_4 + 6\Phi_6) \rangle$. For these correlators, the change of signal reflects mainly the selection on the collision geometry. In some other cases, results differ significant between q_n^S and ϵ_n selections, such as $\langle \cos 4(\Phi_2^A - \Phi_4^C) \rangle$, $\langle \cos 6(\Phi_2^A - \Phi_6^C) \rangle$ and $\langle \cos(2\Phi_2^B + 3\Phi_3^A - 5\Phi_5^C) \rangle$ between q_2^S and ϵ_2 , and $\langle \cos(2\Phi_2^B + 3\Phi_3^A - 5\Phi_5^C) \rangle$ and $\langle \cos(2\Phi_2^A + 3\Phi_3^B - 5\Phi_5^C) \rangle$ between q_3^S and ϵ_3 . For these correlators, the change of signal are probably also affected by the dynamical fluctuations present in the AMPT model.
- For some event plane correlators, the signal for different types show very different dependence on q_2^S . For example $\langle \cos(2\Phi_2^A - 6\Phi_3^C + 4\Phi_4^B) \rangle$ and $\langle \cos(2\Phi_2^C - 6\Phi_3^A + 4\Phi_4^B) \rangle$ has opposite dependence, and both differs from the dependence on ϵ_2 . This may be a result of the rapidity fluctuations of $v_3(\eta)$, as shown in Figure 8.

Heavy ion collision at RHIC and LHC is a finite number system. A typical Pb+Pb collision involves a few hundred colliding nucleons and produces on the order of 10,000 particles in the final state. Both the collision geometry defined by the nucleons and the collective expansion of produced particles can fluctuate strongly event-by-event. It remains a challenge to disentangle the fluctuations at the initial state and dynamical fluctuations generated in the collective expansion, a prerequisite for understanding the physics behind these fluctuations. Future progress requires a detailed and systematic study of the correlations between all v_n and their phases Φ_n : $p(v_n, v_m, \dots, \Phi_n, \Phi_m, \dots)$, in order to disentangle different sources of fluctuations. The study presented in this paper attempts to establish the methodology for accessing these correlations and provides the initial guidance on how these correlations are connected to the initial geometry and dynamics in the collective expansion. Much more theoretical efforts, especially those based on the application of event shape selection technique in EbyE hydrodynamics, will provide more realistic and detailed insights on the nature of the fluctuations and non-linear dynamics in various stages of the heavy ion collisions.

This research is supported by NSF under grant number PHY-1019387 and PHY-1305037.

- [1] G.-Y. Qin, H. Petersen, S. A. Bass, and B. Muller, *Phys.Rev.* **C82**, 064903 (2010), arXiv:1009.1847 [nucl-th]
- [2] D. Teaney and L. Yan, *Phys.Rev.* **C83**, 064904 (2011), arXiv:1010.1876 [nucl-th]
- [3] Z. Qiu and U. W. Heinz, *Phys.Rev.* **C84**, 024911 (2011), arXiv:1104.0650 [nucl-th]
- [4] F. G. Gardim, F. Grassi, M. Luzum, and J.-Y. Ollitrault, *Phys.Rev.* **C85**, 024908 (2012), arXiv:1111.6538 [nucl-th]
- [5] D. Teaney and L. Yan, *Phys.Rev.* **C86**, 044908 (2012), arXiv:1206.1905 [nucl-th]
- [6] F. G. Gardim, F. Grassi, M. Luzum, and J.-Y. Ollitrault, *Phys.Rev.* **C87**, 031901 (2013), arXiv:1211.0989 [nucl-th]
- [7] R. S. Bhalerao, M. Luzum, and J.-Y. Ollitrault, *Phys.Rev.* **C84**, 034910 (2011), arXiv:1104.4740 [nucl-th]
- [8] G.-Y. Qin and B. Muller, *Phys.Rev.* **C85**, 061901 (2012), arXiv:1109.5961 [hep-ph]
- [9] J. Jia and S. Mohapatra, *Eur.Phys.J.* **C73**, 2510 (2013), arXiv:1203.5095 [nucl-th]
- [10] A. Adare *et al.* (PHENIX), *Phys.Rev.Lett.* **107**, 252301 (2011), arXiv:1105.3928 [nucl-ex]
- [11] L. Adamczyk *et al.* (STAR), (2013), arXiv:1301.2187 [nucl-ex]
- [12] K. Aamodt *et al.* (ALICE), *Phys.Lett.* **B708**, 249 (2012), arXiv:1109.2501 [nucl-ex]
- [13] G. Aad *et al.* (ATLAS), *Phys.Rev.* **C86**, 014907 (2012), arXiv:1203.3087 [hep-ex]
- [14] S. Chatrchyan *et al.* (CMS), *Eur.Phys.J.* **C72**, 2012 (2012), arXiv:1201.3158 [nucl-ex]
- [15] G. Aad *et al.* (ATLAS), (2013), arXiv:1305.2942 [hep-ex]
- [16] ATLAS, *Nucl. Phys. A* **910**, 276 (2013), ATLAS-CONF-2012-049, <https://cds.cern.ch/record/1451882>, arXiv:1208.1427 [nucl-ex]
- [17] K. Aamodt *et al.* (ALICE), *Phys.Rev.Lett.* **107**, 032301 (2011), arXiv:1105.3865 [nucl-ex]
- [18] Z. Qiu and U. Heinz, *Phys.Lett.* **B717**, 261 (2012), arXiv:1208.1200 [nucl-th]
- [19] D. Teaney and L. Yan, *Nucl.Phys.A904-905* **2013**, 365c (2013), arXiv:1210.5026 [nucl-th]
- [20] R. S. Bhalerao, J.-Y. Ollitrault, and S. Pal, *Phys. Rev. C* **88**, 024909, 024909 (2013), arXiv:1307.0980 [nucl-th]
- [21] J. Schukraft, A. Timmins, and S. A. Voloshin, *Phys.Lett.* **B719**, 394 (2013), arXiv:1208.4563 [nucl-ex]
- [22] H. Petersen and B. Muller, *Phys.Rev.* **C88**, 044918 (2013), arXiv:1305.2735 [nucl-th]
- [23] R. A. Lacey, D. Reynolds, A. Taranenko, N. Ajitanand, J. Alexander, *et al.*, (2013), arXiv:1311.1728 [nucl-ex]
- [24] L. Pang, Q. Wang, and X.-N. Wang, *Phys.Rev.* **C86**, 024911 (2012), arXiv:1205.5019 [nucl-th]
- [25] H. Petersen, V. Bhattacharya, S. A. Bass, and C. Greiner, *Phys.Rev.* **C84**, 054908 (2011), arXiv:1105.0340 [nucl-th]
- [26] K. Xiao, F. Liu, and F. Wang, *Phys.Rev.* **C87**, 011901 (2013), arXiv:1208.1195 [nucl-th]
- [27] Z.-W. Lin, C. M. Ko, B.-A. Li, B. Zhang, and S. Pal, *Phys.Rev.* **C72**, 064901 (2005), arXiv:nucl-th/0411110 [nucl-th]
- [28] J. Xu and C. M. Ko, *Phys.Rev.* **C84**, 044907 (2011), arXiv:1108.0717 [nucl-th]
- [29] J. Xu and C. M. Ko, *Phys.Rev.* **C84**, 014903 (2011),

- arXiv:1103.5187 [nucl-th]
- [30] G.-L. Ma and X.-N. Wang, *Phys.Rev.Lett.* **106**, 162301 (2011), arXiv:1011.5249 [nucl-th]
- [31] J. Xu and C. M. Ko, *Phys.Rev.* **C83**, 034904 (2011), arXiv:1101.2231 [nucl-th]
- [32] L. Pang, Q. Wang, and X.-N. Wang, *Nucl.Phys.* **A904-905**, 811c (2013), arXiv:1211.1570 [nucl-th]
- [33] J. Jia and S. Mohapatra, *Phys.Rev.* **C88**, 014907 (2013), arXiv:1304.1471 [nucl-ex]
- [34] A. M. Poskanzer and S. Voloshin, *Phys.Rev.* **C58**, 1671 (1998), arXiv:nucl-ex/9805001 [nucl-ex]
- [35] M. Luzum and J.-Y. Ollitrault, *Phys.Rev.* **C87**, 044907 (2013), arXiv:1209.2323 [nucl-ex]
- [36] J. Jia and D. Teaney, *Eur.Phys.J.* **C73**, 2558 (2013), arXiv:1205.3585 [nucl-ex]
- [37] A. Bzdak and D. Teaney, *Phys.Rev.* **C87**, 024906 (2013), arXiv:1210.1965 [nucl-th]
- [38] L. Pang, Q. Wang, and X.-N. Wang, (2013), arXiv:1309.6735 [nucl-th]

Appendix A: Additional figures

Figure 16 compare the $v_n(\eta)$ obtained for lower 10% (top) and upper 10% (bottom) of the q_n^S values and for two different η ranges for the subevent S: $-6 < \eta < -2$ (circles) and $-6 < \eta < -3$ (boxes). The event shape selection is less effective when subevent S has a smaller η range, but the overall η asymmetry is similar between the two cases.

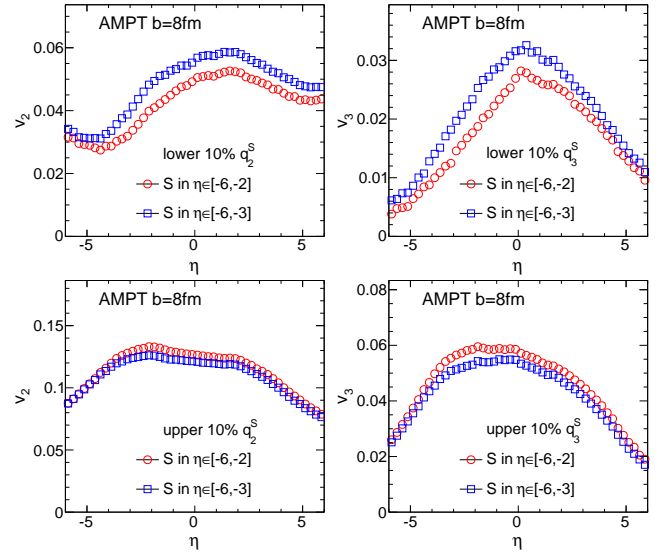


FIG. 16: The $v_2(\eta)$ (left) and $v_3(\eta)$ (right) selected for lower 10% (top) and upper 10% (bottom) of the q_n^S values. The results are shown for the subevent S (used for event shape selection) defined in two η ranges: $-6 < \eta < -2$ (circles) and $-6 < \eta < -3$ (boxes).

For completeness, Figures 17 and 18 provide various

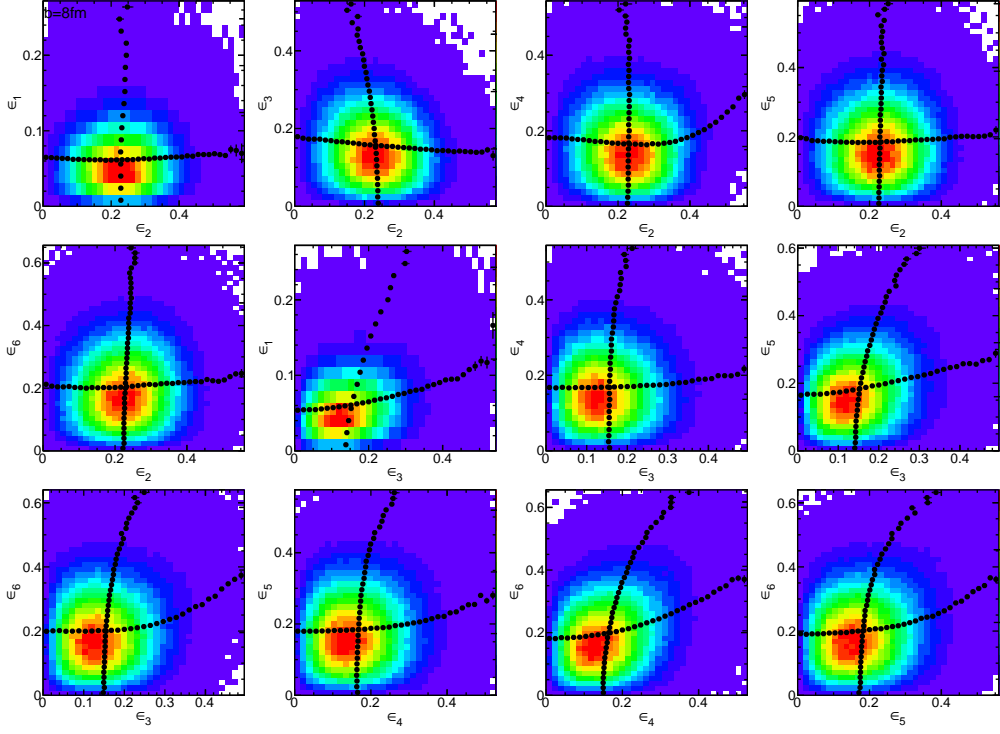


FIG. 17: (Color online) Selected correlations between ϵ_n of different order for Pb+Pb events at $b = 8$ fm.

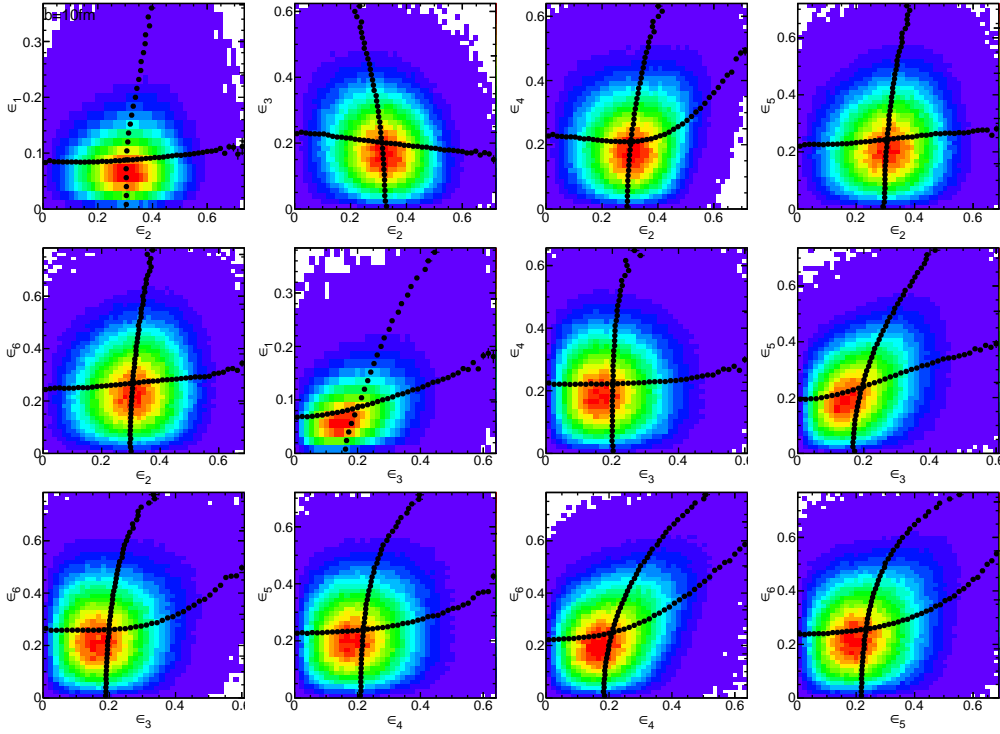


FIG. 18: (Color online) Selected correlations between ϵ_n of different order for Pb+Pb events at $b = 10$ fm.

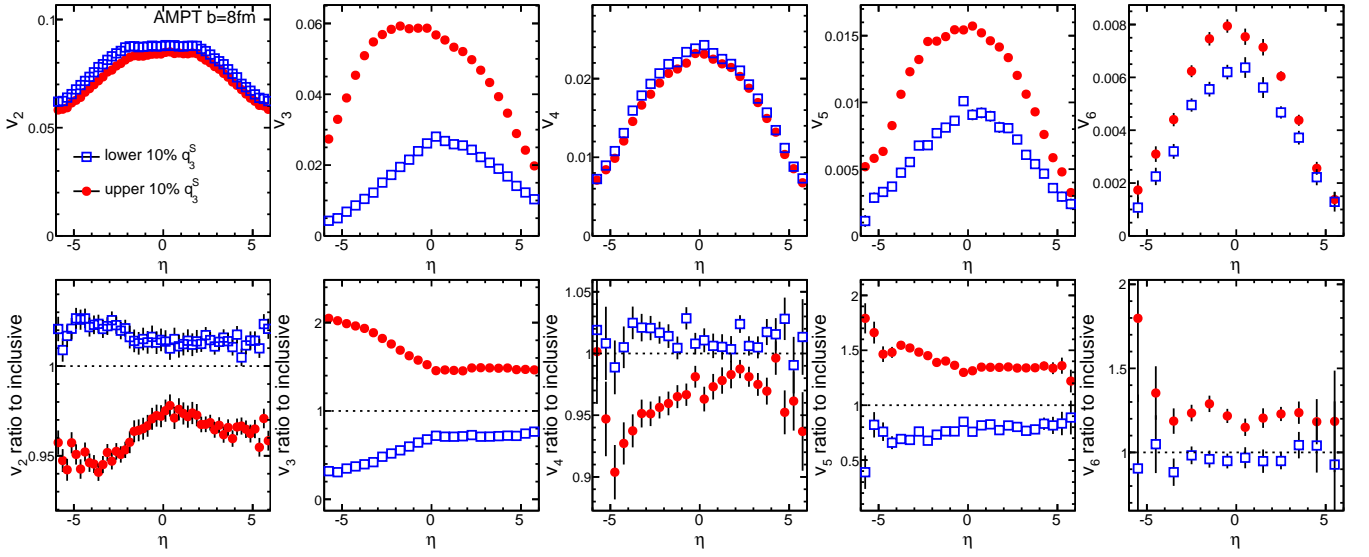


FIG. 19: (Color online) $v_n(\eta)$ for events selected for lower 10% (open symbols) and upper 10% (solid symbols) of the values of q_3^S for AMPT Pb+Pb events with $b = 8$ fm. Results are shown for $v_2(\eta)$, $v_3(\eta)$, $v_4(\eta)$, $v_5(\eta)$, $v_6(\eta)$ from left panel to the right panel. The ratios of $v_n(\eta)$ between events with q_2^S selection to the inclusive events are shown in the bottom panels.

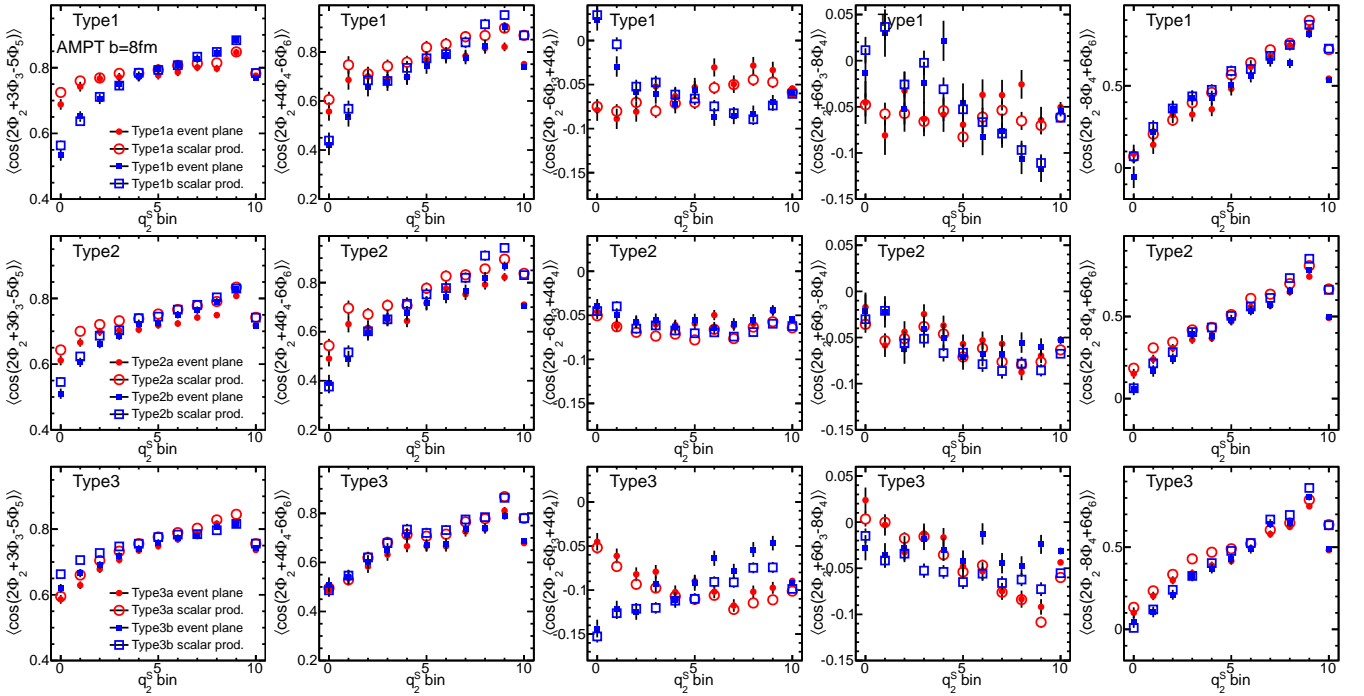


FIG. 20: (Color online) The five three-plane correlators (from left to right) as a function of q_2^S event class for AMPT Pb+Pb events with $b = 8$ fm. The results for the three type groups are shown in different row: Type1a and Type1b (top row), Type2a and Type2b (middle row), Type2a and Type2b (bottom row) and they are compared between the EP method and the SP method. The last bin in each panel shows the result for inclusive events.

correlations between ϵ_n and ϵ_m for AMPT Pb+Pb events with two fixed impact parameters, respectively. Many types of correlations, in addition to those discussed in Section III can be identified. Figure 19 shows the η dependence of the $v_n(\eta)$ for events selected based on the q_3^S .

It shows clearly that the forward/backward asymmetry of $v_5(\eta)$ is strongly correlated with that of the $v_3(\eta)$. The $v_5(\eta)$ also exhibits η -asymmetry similar to that observed for $v_3(\eta)$, despite of the fact that the event shape selection is performed on q_3^S . Figures 20 shows various three-plane

correlators compared between the event plane method and the scalar product method; the dependences on q_2^S

are similar between the two methods.